# Multicomponent volume reconstruction from slice data using a modified multicomponent Cahn–Hilliard system

Yibao Li [a], Jing Wang [b,c], Bingheng Lu [b,c,d], Darae Jeong [e], Junseok Kim [f,*]

[a] *School of Mathematics and Statistics, Xi'an Jiaotong University, Xi'an, 710049, China*
[b] *Collaborative Innovation Center of High-End Manufacturing Equipment, Xi'an Jiaotong University, Xi'an, 710049, China*
[c] *National Institue of Additive Manufacturing, Xi'an, 710049, China*
[d] *School of Mechanical Engineering, Dongguan University of Technology, Dongguan, 523808, China*
[e] *Department of Mathematics, Kangwon National University, Gangwon-do, 24341, Republic of Korea*
[f] *Department of Mathematics, Korea University, Seoul, 02841, Republic of Korea*

## ABSTRACT

We propose an efficient and robust algorithm to reconstruct the volumes of multi-labeled objects from sets of cross sections without overlapping regions, artificial gaps, or mismatched interfaces. The algorithm can handle cross sections wherein different regions have different labels. The present study represents a multicomponent extension of our previous work (Li et al. (2015), [1]), wherein we modified the original Cahn–Hilliard (CH) equation by adding a fidelity term to keep the solution close to the single-labeled slice data. The classical CH equation possesses desirable properties, such as smoothing and conservation. The key idea of the present work is to employ a multicomponent CH system to reconstruct multicomponent volumes without self-intersections. We utilize the linearly stabilized convex splitting scheme introduced by Eyre with the Fourier-spectral method so that we can use a large time step and solve the discrete equation quickly. The proposed algorithm is simple and produces smooth volumes that closely preserve the original volume data and do not self-intersect. Numerical results demonstrate the effectiveness and robustness of the proposed method.

© 2019 Elsevier Ltd. All rights reserved.

## 1. Introduction

Developing efficient and robust three-dimensional (3D) algorithms for volume reconstruction from series of slice data is highly important, because 3D volume reconstruction from sequences of medical images has many practical applications, such as plastic surgery, medical diagnostic systems, treatment planning, anatomy teaching, and virtual surgery systems [1,2] (see Fig. 1(a) and (b)).

Much research work has been dedicated to reconstructing surfaces or volumes from sets of planar cross sections [3–10]. Guo et al. [3] developed a morphology-based interpolation method for 3D medical image reconstruction. The authors of [4] proposed a 3D volume reconstruct algorithm from serial cross sections using spline theory, an elastic interpolation algorithm, and the surface consistency theorem. Jones and Chen [5] presented a surface reconstruction method from a stack of contour slices using only basic geometric properties. Memari and Boissonnat [6]

utilized Delaunay triangulation for a volume constrained by cross-section curves. The authors of [7] presented a shape-based interpolation scheme for multidimensional images. Liu et al. [8] proposed a surface reconstruction method from non-parallel networks. Deng et al. [9] developed a surface reconstruction method for freehand 3D ultrasound based on a variational implicit function. Sharma and Agarwal [10] developed a method for 3D surface reconstruction from unorganized planar cross sections using a level-set function.

Recently, we developed a fast and accurate method for volume reconstruction from a set of slice data [11]. The developed method was based on the Cahn–Hilliard (CH) equation [12], which achieves a good smoothing effect and can be applied to image inpainting problems [13]. By adding a fidelity term, the modified CH equation can obtain a smooth volume while keeping the solution close to the slice data. In the phase-field framework, Bretin et al. [14] proposed a variational approach based on a minimizer of a geometric regularity criterion with inclusion-exclusion constraints associated with the cross sections. All of the above-mentioned reconstruction methods can process one region or separated regions, but cannot process contacting regions. That is, if we reconstruct each region
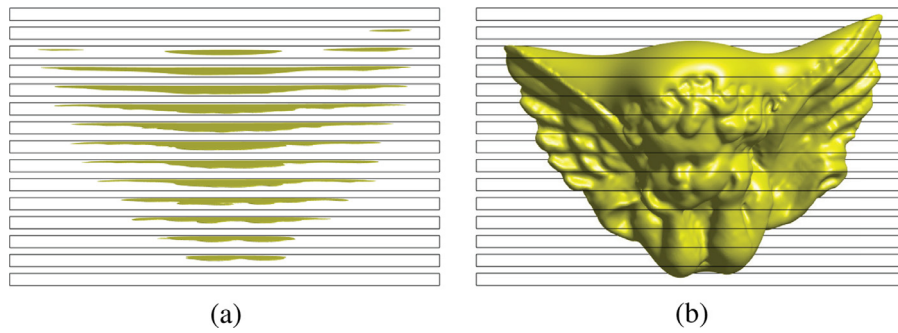
**Fig. 1.** Volume reconstruction procedure from slice data: (a) given slice data and (b) 3D volume reconstruction.
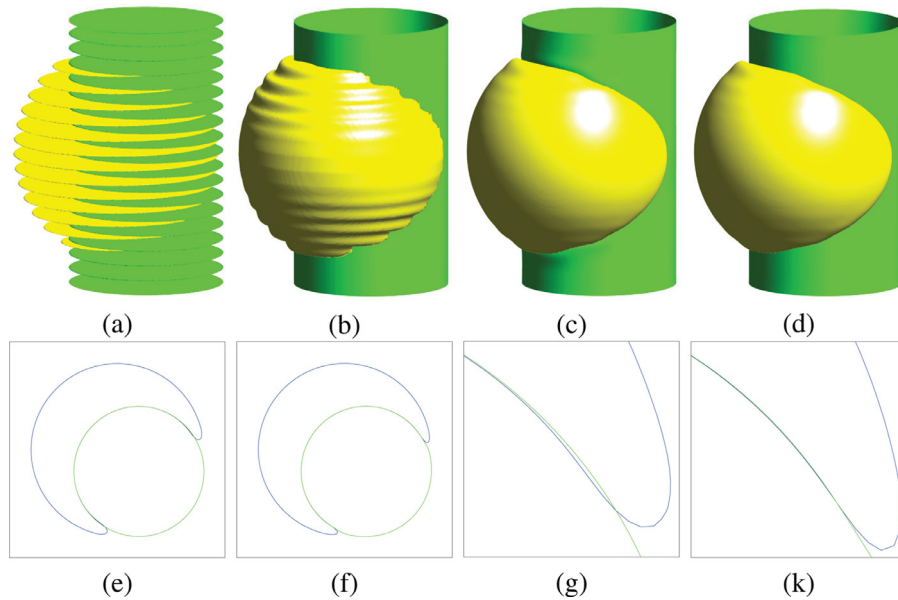


**Fig. 2.** Comparison of the results obtained by applying the binary volume reconstruction method twice and the proposed multicomponent volume reconstruction method. (a) synthetic slice data, (b) initial shape, (c) volume reconstructed using the binary volume reconstruction method twice, and (d) volume reconstructed using the proposed multicomponent volume reconstruction method. (e) and (f) show the half-level contours of (c) and (d) at the middle slice, respectively. (g) and (k) show the closed views of (e) and (f), respectively.
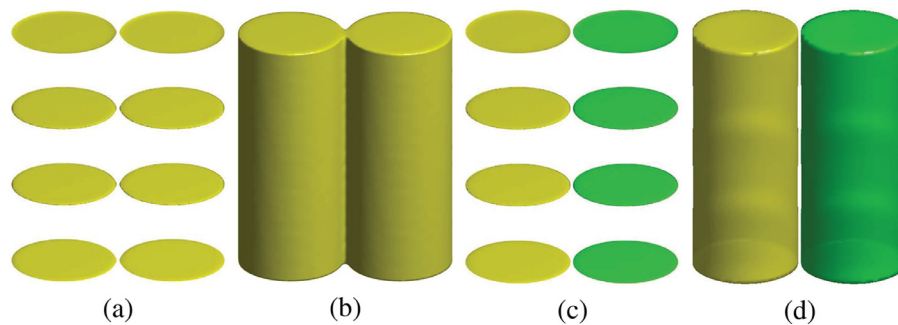


**Fig. 3.** Comparison between the binary and multicomponent volume reconstructions. (a) and (c) show the given slice data. (b) and (d) show the 3D volume reconstructions from (a) and (c), respectively.

separately, then the reconstructed objects may overlap with each other (see Fig. 2).

Therefore, we require an efficient and robust algorithm to reconstruct the 3D volumes of multi-labeled objects from a set of cross sections without overlapping regions. Another application of multicomponent volume reconstruction is to obtain a divided model, where the structures are located relatively close to each other. Fig. 3 shows separated regions merged together in the bi-

nary volume reconstruction framework. On the other hand, the multicomponent volume reconstruction method can keep the region divided. Recently, several approaches [15–18] have been developed to work with multiple models. Bermano et al. [15] used multiple implicit functions to extract multi-labeled material interfaces from sampled planar cross sections of arbitrary orientation. Ju and his collaborators [16–18] developed an efficient topology-controlled reconstruction algorithm to reconstruct a multi-labeled

volume from cross sections. Their algorithms are able to both produce a smooth multi-material interface and simultaneously satisfy the topological requirements. Our proposing method will generate similar results with a simple algorithm. We only solve the governing partial differential equation to reconstruct multi-labeled volumes from cross sections.

For multicomponent volume reconstruction, the proposed method should construct 3D models without overlapping regions, artificial gaps, or mismatched interfaces. In this study, we propose an efficient and robust algorithm to reconstruct 3D volumes of multi-labeled objects from a set of cross sections. The proposed algorithm can handle cross sections in which different regions are classified as having different labels. The present study represents an extension of our previous work [11]. The main contribution of the present work is to reconstruct multicomponent volumes without self-intersections or gaps.

The remainder of this paper is organized as follows. In Section 2, we briefly review our previous method for binary 3D reconstruction. Section 3 describes the proposed method for multicomponent 3D reconstruction. In Section 4, we describe a practically stabilized convex splitting scheme for volume reconstruction, and present an efficient and robust numerical method based on a Fourier-spectral method. In Section 5, we present various numerical experiments to demonstrate the efficiency and robustness of the proposed algorithm. Finally, our conclusions are provided in Section 6.

## 2. Binary 3D reconstruction

We briefly review a numerical method [11] for single component volume reconstruction using a set of slice data, which will be extended to a multicomponent volume reconstruction algorithm. In the single component volume reconstruction algorithm, we first perform image segmentation for the given slice data using a modified Allen–Cahn (AC) equation [19–21]. Note that there exists a level-set-based image segmentation method [22,23]. Next, we reconstruct the volume using a modified CH equation. Let $S_l$ for $l = 1, \ldots, N_l$ be the given two-dimensional slice data at $z = Z_l$, where $N_l$ is the number of slice data sets. For example, medical slice data can be obtained from MR images [24]. Let $\psi(x, y, Z_l)$ be the two-dimensional segmented data obtained using the image segmentation method, the modified AC equation, on $S_l$. For simplicity, we assume that the 3D domain is given as $\Omega = \{\mathbf{x} = (x, \ y, \ z) | \ x \in (0, L_x), \ y \in (0, L_y), \ z \in (0, L_z)\}$. For $(x, y, z) \in \Omega$, let

$$\psi(x, y, z) = \begin{cases} \psi(x, y, Z_l), & \text{if } z = Z_l, \\ 0, & \text{otherwise.} \end{cases}$$

be the fidelity term. To obtain a volume fraction function $\phi$ and retrieve the surface as a level set of the function $\phi$, we use the following modified CH equation with a fidelity term:

$$\frac{\partial \phi(\mathbf{x}, t)}{\partial t} = \Delta \mu(\mathbf{x}, t) + \lambda(\mathbf{x})(\psi(\mathbf{x}) - \phi(\mathbf{x}, t)), \quad \mathbf{x} \in \Omega, \ 0 < t \leq T, \ (1)$$

$$\mu(\mathbf{x}, t) = F'(\phi(\mathbf{x}, t)) - \epsilon^2 \Delta \phi(\mathbf{x}, t), \tag{2}$$

$$\phi(\mathbf{x}, 0) = \phi^0(\mathbf{x}), \tag{3}$$

where $F(\phi) = 0.25\phi^2(\phi - 1)^2$, $\epsilon$ is a positive constant, and

$$\lambda(x, y, z) = \begin{cases} \lambda^0, & \text{if } z = Z_l, \\ 0, & \text{otherwise.} \end{cases}$$

Here, $\phi(\mathbf{x}, t)$ is a phase-field function, which takes values of approximately 1 and 0 in the reconstructed volume's interior and exterior regions, respectively. Furthermore, $\phi(\mathbf{x}, t) = 0.5$ represents the interface of the two phases. The zero Neumann boundary conditions are applied as the boundary conditions on $\phi$ and $\mu$: $\mathbf{n} \cdot \nabla \phi = \mathbf{n} \cdot \nabla \mu = 0$ on $\partial \Omega$, where $\mathbf{n}$ is the unit normal vector on the domain boundary. With an initial condition $\phi^0(\mathbf{x})$, we apply a linear interpolation between two consecutive slices as

$$\phi^0(x, y, z) = \theta \psi(x, y, Z_{l+1}) + (1 - \theta) \psi(x, y, Z_l), \ z \in [Z_l, Z_{l+1}], (4)$$

Here, $\theta = (z - Z_l)/(Z_{l+1} - Z_l)$ for $l = 1, \ldots, N_l - 1$. The surface of the volume is represented by the half-level set of $\phi$. See Fig. 1(b) for the reconstructed surface. If $\lambda^0 = 0$, then Eqs. (1) and (2) become the classical CH equation [12], which was proposed as a mathematical equation representing the phase separation, and has been widely employed to model many scientific phenomena, such as image inpainting, spinodal decomposition, tumor growth, multi-phase fluid flows, topology optimization, and microstructure formations. See [25,26] and references therein for fundamental principles, useful applications, and physical, mathematical, and numerical derivations of the CH equation. Eqs. (1) and (2) in the two-dimensional space have been applied to the image inpainting problem [13], and here we apply this approach to the 3D volume reconstruction problem.

## 3. Multicomponent 3D reconstruction

We propose a robust and efficient numerical method for multicomponent volume reconstruction using a set of slice data. We consider an $N$-component mixture in a domain $\Omega \subset \mathbf{R}^3$. Let $\phi_i = \phi_i(\mathbf{x}, t)$ for $i = 1, \ldots, N$ be the concentration of each component in the system. Here, $\mathbf{x}$ and $t$ are the space and time variables, respectively. The total sum of the components must be equal to 1, i.e., $\sum_{i=1}^{N} \phi_i = 1$. Let $\boldsymbol{\phi} = (\phi_1, \phi_2, \ldots, \phi_N)$ be a vector-valued phase field. The total free energy is given as

$$\mathcal{E}(\boldsymbol{\phi}) = \int_\Omega \left( F(\boldsymbol{\phi}) + \frac{\epsilon^2}{2} \sum_{i=1}^{N} |\nabla \phi_i|^2 \right) d\mathbf{x}, \tag{5}$$

where $F(\phi) = \sum_{i=1}^{N} \phi_i^2(\phi_i - 1)^2/4$ is the free-energy. The temporal evolution of $\boldsymbol{\phi}$ is governed by the following multicomponent CH system [25,27,28]:

$$\frac{\partial \phi_i}{\partial t} = \Delta \left( f(\phi_i) + \bar{\beta}_i(\boldsymbol{\phi}) - \epsilon^2 \Delta \phi_i \right), \quad i = 1, \ldots, N, \tag{6}$$

where

$$f(\phi_i) = \frac{\partial F(\boldsymbol{\phi})}{\partial \phi_i} = \phi_i(\phi_i - 0.5)(\phi_i - 1) \text{ and } \bar{\beta}_i(\boldsymbol{\phi})$$

$$= -\frac{1}{N} \sum_{j=1}^{N} f(\phi_j). \tag{7}$$

This variable Lagrangian multiplier enforces that the constraint $\sum_{i=1}^{N} \phi_i = 1$ is satisfied for both space and time. An alternative choice for the Lagrangian multiplier is $\bar{\beta}_i(\boldsymbol{\phi}) = -\phi_i \sum_{j=1}^{N} f(\phi_j)$, which has the desirable property of preserving small features [29,30]. The Lagrangian multiplier satisfies the following properties:

$$\frac{\partial}{\partial t} \sum_{i=1}^{N} \phi_i = \sum_{i=1}^{N} \frac{\partial \phi_i}{\partial t} = \Delta \left( \sum_{i=1}^{N} f(\phi_i) + \sum_{i=1}^{N} \bar{\beta}_i(\boldsymbol{\phi}) - \epsilon^2 \Delta \sum_{i=1}^{N} \phi_i \right)$$

$$= \Delta \left( \sum_{i=1}^{N} f(\phi_i) + \sum_{i=1}^{N} \bar{\beta}_i(\boldsymbol{\phi}) \right) = 0. \tag{8}$$

Fig. 4 illustrates the evolution of the multicomponent CH equation for two overlapping circles in two-dimensional space. From
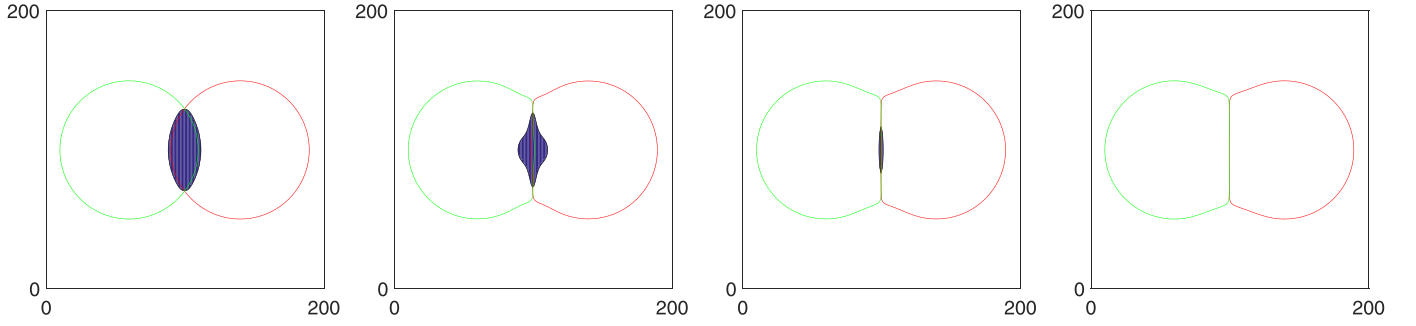
**Fig. 4.** The evolution of the multicomponent CH equation for two overlapping circles in two-dimensional space. From left to right, the snapshots are from $t = 0$, 1000, 2000, and 3000. The green and red lines represent the interface of the two phases. The blue region represents $\beta > 0.05$. For interpretation of the references to color in this figure, the reader is referred to the web version of this article. (For interpretation of the references to color in this figure legend, the reader is referred to the web version of this article.)

left to right, the snapshots represent $t = 0$, 1000, 2000, and 3000. The green and red lines represent the interface of the two phases. The blue region represents $\beta > 0.05$. We can see that the variable Lagrangian multiplier $\beta$ prevents the occurrence of self intersections. Furthermore, when the overlapping region is separated, $\beta$ becomes smaller than 0.05. Finally, we propose the following modified multicomponent CH equation for multicomponent volume reconstruction:

$$\frac{\partial \phi_i}{\partial t} = \Delta \big[ f(\phi_i) + \bar{\beta}_i(\boldsymbol{\phi}) - \epsilon^2 \Delta \phi_i \big] + \lambda_i(\psi_i - \phi_i) \quad \text{for } i = 1, \ldots, N, \quad (9)$$

where

$$\lambda_i(\mathbf{x}) = \begin{cases} \lambda_i^0, & \text{if } \mathbf{x} \text{ is in the given slice data for } i\text{th component,} \\ 0, & \text{otherwise.} \end{cases}$$

Here, $\lambda_i^0$ is a positive constant for the $i$th component. The zero Neumann boundary conditions are applied: $\nabla \phi_i \cdot \mathbf{n} = 0$ on $\partial \Omega$, where $\mathbf{n}$ is the unit normal vector to $\partial \Omega$. In the cross sections, the different regions are classified as having different labels $\psi_i$, where these labels represent the concentration of each component in the system and satisfies

$$\sum_{i=1}^{N} \psi_i = 1. \tag{10}$$

The fidelity term $\lambda_i(\psi_i - \phi_i)$ in Eq. (9) can be obtained by a gradient flow under an $L^2$-inner product for the energy, $\int_{\Omega} \sum_{i=1}^{N} 0.5 \lambda_i (\psi_i - \phi_i)^2 d\mathbf{x}$ [31]. Taking a summation on both sides of Eq. (9), we obtain

$$0 = \frac{\partial}{\partial t} \sum_{i=1}^{N} \phi_i = \sum_{i=1}^{N} \Big( \Delta \big[ f(\phi_i) + \bar{\beta}_i(\phi) - \epsilon^2 \Delta \phi_i \big] + \lambda_i(\psi_i - \phi_i) \Big)$$

$$= \begin{cases} \lambda^0 \big( \sum_{i=1}^{N} \psi_i - \sum_{i=1}^{N} \phi_i \big), & \text{if } \mathbf{x} \text{ is in the given slice} \\ & \text{data for } i\text{th component,} \\ 0, & \text{otherwise.} \end{cases}$$

Here, we have applied Eqs. (8) and (10), $\lambda_i^0 = \lambda^0$, and the property $\sum_{i=1}^{N} \phi_i = 1$.

## 4. Numerical method

We employ the linearly stabilized splitting scheme introduced by Eyre [32] with the Fourier-spectral method [33], which allows for large time steps. We assume that there are $N_l$ slices with $N_x \times N_y$ pixels on the 3D space $\Omega = (0, L_x) \times (0, L_y) \times (0, L_z)$, where $N_x$ and $N_y$ are even integers. Let $N_z = N_l + (N_l - 1)I$, where $I$ is the number of slices inserted between consecutive slice data sets. Note that if $N_l + (N_l - 1)I$ is odd, then we set $N_z = (N_l -$

$1)(I + 1)$, which implies that we use $I$ slices between any two given successive slice data sets except for $I - 1$ slices for the first two sets. Let $x_m = (2m - 1)L_x/(2N_x)$, $y_n = (2n - 1)L_y/(2N_y)$, $z_k = (2k - 1)L_z/(2N_z)$, for $1 \leq m \leq N_x$, $1 \leq n \leq N_y$, and $1 \leq k \leq N_z$, where $N_z$ is an even integer. Furthermore, let $\phi_{i,mnk}^s$ be an approximation of $\phi_i(x_m, y_n, z_k, s\Delta t)$, where $\Delta t$ is the time step. The discrete cosine transform $\hat{\phi}_{i,pqr}^s$ for $p = 1, \ldots, N_x$, $q = 1, \ldots, N_y$, and $r = 1, \ldots, N_z$ is defined as

$$\hat{\phi}_{i,pqr}^s = \alpha_p \beta_q \gamma_r \sum_{m=1}^{N_x} \sum_{n=1}^{N_y} \sum_{k=1}^{N_z} \phi_{i,mnk}^s \cos(x_m \pi \xi_p) \cos(y_n \pi \eta_q) \cos(z_k \pi \nu_r),$$

where

$$\alpha_p = \begin{cases} \sqrt{1/N_x}, & p = 1 \\ \sqrt{2/N_x}, & 2 \leq p \leq N_x \end{cases}, \quad \beta_q = \begin{cases} \sqrt{1/N_y}, & q = 1 \\ \sqrt{2/N_y}, & 2 \leq q \leq N_y \end{cases},$$

$$\gamma_r = \begin{cases} \sqrt{1/N_z}, & r = 1 \\ \sqrt{2/N_z}, & 2 \leq r \leq N_z. \end{cases}$$

The variables $\xi_p$, $\eta_q$, and $\nu_r$ are defined as $\xi_p = (p - 1)/L_x$, $\eta_q = (q - 1)/L_y$, and $\nu_r = (r - 1)/L_z$, respectively. The inverse discrete cosine transform is

$$\phi_{i,mnk}^s = \sum_{p=1}^{N_x} \sum_{q=1}^{N_y} \sum_{r=1}^{N_z} \alpha_p \beta_q \gamma_r \hat{\phi}_{i,pqr}^s \cos(\xi_p \pi x_m) \cos(\eta_q \pi y_n) \cos(\gamma_r \pi z_k). \tag{11}$$

We apply the linearly stabilized splitting scheme [32] to Eq. (9):

$$\frac{\phi_{i,mnk}^{s+1} - \phi_{i,mnk}^s}{\Delta t} = \Delta \big( f(\phi_{i,mnk}^s) - 2\phi_{i,mnk}^s + 2\phi_{i,mnk}^{s+1}$$
$$+ \bar{\beta}_{i,mnk}^s - \epsilon^2 \Delta \phi_{i,mnk}^{s+1} \big)$$
$$+ \lambda_{i,mnk}(\psi_{i,mnk} - \phi_{i,mnk}^s). \tag{12}$$

Thus, Eq. (12) can be transformed into the discrete cosine space as follows:

$$\frac{\hat{\phi}_{i,pqr}^{s+1} - \hat{\phi}_{i,pqr}^s}{\Delta t} = -\big[ (\xi_p \pi)^2 + (\eta_q \pi)^2 + (\gamma_r \pi)^2 \big]$$
$$\times \Big( \hat{f}_{i,pqr}^s - 2\hat{\phi}_{i,pqr}^s + 2\hat{\phi}_{i,pqr}^{s+1} + \hat{\bar{\beta}}_{i,pqr}^s$$
$$+ \epsilon^2 [(\xi_p \pi)^2 + (\eta_q \pi)^2 + (\gamma_r \pi)^2] \hat{\phi}_{i,pqr}^{s+1} \Big) + \hat{g}_{i,pqr}^s.$$

Here, we have employed the discrete cosine transform for the Laplacian operator, which is defined as

$$\Delta \hat{\phi}_{i,pqr}^s = -[(\xi_p \pi)^2 + (\eta_q \pi)^2 + (\gamma_r \pi)^2] \hat{\phi}_{i,pqr}^s.$$

Furthermore, $\hat{f}_{i,pqr}^s$, $\hat{\bar{\beta}}_{i,pqr}^s$, and $\hat{g}_{i,pqr}^s$ denote the discrete cosine

transforms of $f(\phi^s_{i,mnk})$, $\bar{\beta}^s_{i,mnk}$, and $\lambda_{i,mnk}(\psi_{i,mnk} - \phi^s_{i,mnk})$, respectively. Therefore, we obtain the following discrete cosine transform

$$\hat{\phi}^{s+1}_{i,pqr} = \frac{\hat{\phi}^s_{i,pqr} + \Delta t \hat{g}^s_{i,pqr} - [(\xi_p\pi)^2 + (\eta_q\pi)^2 + (\gamma_r\pi)^2]\Delta t(\hat{f}^s_{pqr} + \hat{\bar{\beta}}^s_{pqr} - 2\hat{\phi}^s_{pqr})}{1 + 2[(\xi_p\pi)^2 + (\eta_q\pi)^2 + (\gamma_r\pi)^2]\Delta t + \epsilon^2[(\xi_p\pi)^2 + (\eta_q\pi)^2 + (\gamma_r\pi)^2]^2\Delta t}.$$

The corresponding function $\phi^{s+1}_{i,mnk}$ can be computed using Eq. (11). The main contributions of the proposed method include the following. (i) The proposed method can construct 3D volumes without artificial gaps and noises because it uses the multicomponent CH system; (ii) the proposed method can obtain 3D volumes without overlapping regions and mismatched interfaces, because the different regions are classified as having different labels, and our method satisfies $\sum_{i=1}^{N} \phi_i = 1$; (iii) the proposed numerical method in Eq. (12) can achieve fast convergence; and (iv) the proposed algorithm is simple to implement.

## 5. Numerical results

In this section, we present numerical examples that demonstrate the efficiency and quality of our proposed multicomponent volume reconstruction algorithm. In particular, we show that our method easily handles topological changes, and performs quickly with non-uniform and noisy data. We regard a numerical result as a steady state solution if the relative error for every component, i.e., $\|\phi^{s+1}_i - \phi^s_i\|_2/\|\phi^s_i\|_2$ for $i = 1, \ldots, N$, is less than a tolerance $tol$. Here, $\|\cdot\|_2$ denotes the discrete $l_2$-norm. Unless otherwise specified, we set $\epsilon = \epsilon_m = m/[4\sqrt{2}\tanh^{-1}(0.9)])$ [26], $L_x = N_x$, $L_y = N_y$, and $L_z = N_z$. The last term in Eq. (9) is a fidelity term that enforces that the updated value ($\phi$) is equal to the given value ($\psi$). Furthermore, $\lambda_i$ balances the diffusion and fidelity terms. By ignoring the effect of diffusion in Eq. (9), we obtain

$$\frac{\partial \phi_i}{\partial t} = \lambda_i(\psi_i - \phi_i). \tag{13}$$

Because Eq. (13) is a separable ordinary differential equation, i.e., $\lambda_i dt + \frac{1}{\phi_i - \psi_i}d\phi_i = 0$, we obtain the following solution with the initial condition $\phi^s_i$:

$$\phi^{s+1}_i = \psi_i + e^{-\lambda_i \Delta t}(\phi^s_i - \psi_i). \tag{14}$$

As shown in Fig. 5, if $\lambda^0$ is larger than $5/\Delta t$, then $\phi^{s+1} \approx \psi$ for any time, which implies that even smaller noises will remain present. We can also derive that if $\lambda^0 < 0.1/\Delta t$, then $\phi^{s+1}$ differs more from $\psi$, which implies that the numerical solution obtained by our proposed method cannot preserve the original topological shape. Therefore, we suggest setting $0.1/\Delta t < \lambda^0 < 5/\Delta t$.
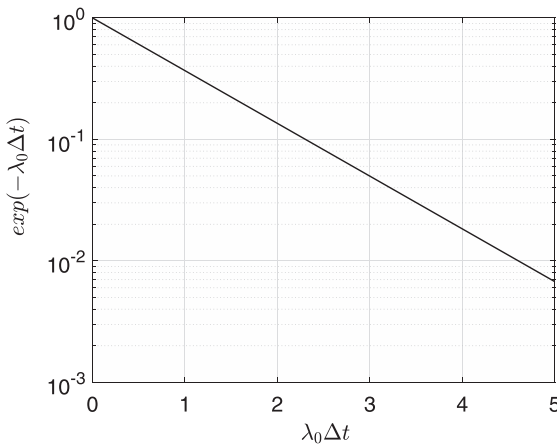
Fig. 6(a)–(c) show the slice data with 5% salt and pepper noise, the initial shape with the interpolation, and the exact solution, respectively. By setting $\lambda_0 = 10$ and $\epsilon = \epsilon_6$, we can remove the noise from the original volume and reconstruct a good volume (see Fig. 6(d)). If $\lambda^0$ is too large, then the fitting term is dominant, and the restored volume tends to become the original one with noise (see Fig. 6(e)). As shown in Fig. 6(f), if $\lambda^0$ is too small, then the motion by diffusion is dominant, and the reconstructed volume is overly smooth. For a fixed $\lambda^0 = 10$, we take the same initial condition except for different $\epsilon = \epsilon_2$ and $\epsilon = \epsilon_{20}$. From the results shown in Fig. 6(g) and (h), we can observe that when $\epsilon$ is too small, the interfacial transition is too sharp. On the other hand, if $\epsilon$ is too large, then the details of the volume are lost. Therefore, we set the time step $\Delta t = 0.1$, $\lambda^0 = 10$, and $tol = 0.001$. For simplicity, we define the volume of each component as $\{\phi_i \geq 1/2\}$. The proposed algorithm is implemented in MATLAB and tested on a 3.4 GHz PC with 16GB main memory. The CPU time is measured in seconds. Table 1 presents the information on the numbers of data points, iteration numbers, and CPU times. We can observe that the proposed method achieves fast convergence.

Fig. 7 shows the average CPU times (in seconds) against $N_x N_y N_z \log(N_x N_y N_z)$. Here, the average CPU time is defined as the total CPU time over all time iterations and the number of components. To demonstrate the convergence rate, we present the fitting plots together. The result suggests that our proposed method achieves $O(N_x N_y N_z \log(N_x N_y N_z))$ efficiency owing to the fast Fourier transform solver.

The following numerical example is performed to demonstrate the quality of our proposed method. Here, three synthetic functions are implicitly defined, for which we can actually compute the errors using a theoretical analysis:

$$\psi(\mathbf{x}) = \tanh[(25 - \sqrt{(x-40)^2 + (y-90)^2})/(\sqrt{2}\epsilon)],$$

$$\psi(\mathbf{x}) = \tanh[(12 - \sqrt{(x-40)^2 + (y-40)^2} + 0.1z)/(\sqrt{2}\epsilon)],$$

$$\psi(\mathbf{x}) = \tanh[(32 - \sqrt{(x-90)^2 + (y-64)^2 + (z-64)^2})/(\sqrt{2}\epsilon)].$$

The domain $\Omega = (0, 128) \times (0, 128) \times (0, 130)$ is utilized. We take 26 slices obtained using the given synthetic function $\psi(\mathbf{x})$. We insert four slices between any two consecutive slice data sets. The simulation is run up to 11 iterations and takes 36.41 s, which implies that our method achieves the reconstruction very quickly. From left to right, the first two figures in Fig. 8 show the zero-isosurfaces of the numerical solution from different views. The second two figures present a comparison between the reference



**Fig. 5.** Logplot of $e^{-\lambda^0\Delta t}$ via $\lambda^0\Delta t$.

**Table 1**
List of data information, iterations, numbers of components, and CPU times (second). 'CPU' is the time required to process the volume reconstruction, $I$ is the number of inserted slices between consecutive slice data sets, and 'NC' is the number of components.

| Case | $(N_x \times N_y, N_l)$ | $I$ | Used Grid size | Iteration | NC | CPU |
|------|------------------------|-----|----------------|-----------|-----|------|
| Fig. 8 | $(128 \times 128, 26)$ | 4 | $128 \times 128 \times 126$ | 11 | 3 | 36.41 |
| Fig. 10 | $(256 \times 256, 26)$ | 4 | $256 \times 256 \times 126$ | 8 | 5 | 108.72 |
| Fig. 11(b) | $(164 \times 178, 105)$ | 1 | $164 \times 178 \times 208$ | 15 | 2 | 103.18 |
| Fig. 11(c) | $(164 \times 178, 53)$ | 3 | $164 \times 178 \times 208$ | 14 | 2 | 98.52 |
| Fig. 11(d) | $(164 \times 178, 35)$ | 5 | $164 \times 178 \times 204$ | 17 | 2 | 129.85 |
| Fig. 12(b) | $(236 \times 342, 28)$ | 1 | $236 \times 342 \times 54$ | 5 | 2 | 28.12 |
| Fig. 12(c) | $(236 \times 342, 28)$ | 5 | $236 \times 342 \times 162$ | 20 | 2 | 117.45 |
| Fig. 13 | $(168 \times 210, 43)$ | 4 | $168 \times 210 \times 210$ | 6 | 2 | 92.13 |
| Fig. 14 | $(128 \times 128, 33)$ | 3 | $128 \times 128 \times 128$ | 12 | 2 | 30.898 |
| Fig. 15 | $(196 \times 416, 54)$ | 3 | $196 \times 416 \times 212$ | 18 | 3 | 234.80 |
| Fig. 16 | $(370 \times 270, 70)$ | 2 | $370 \times 270 \times 208$ | 10 | 5 | 353.85 |
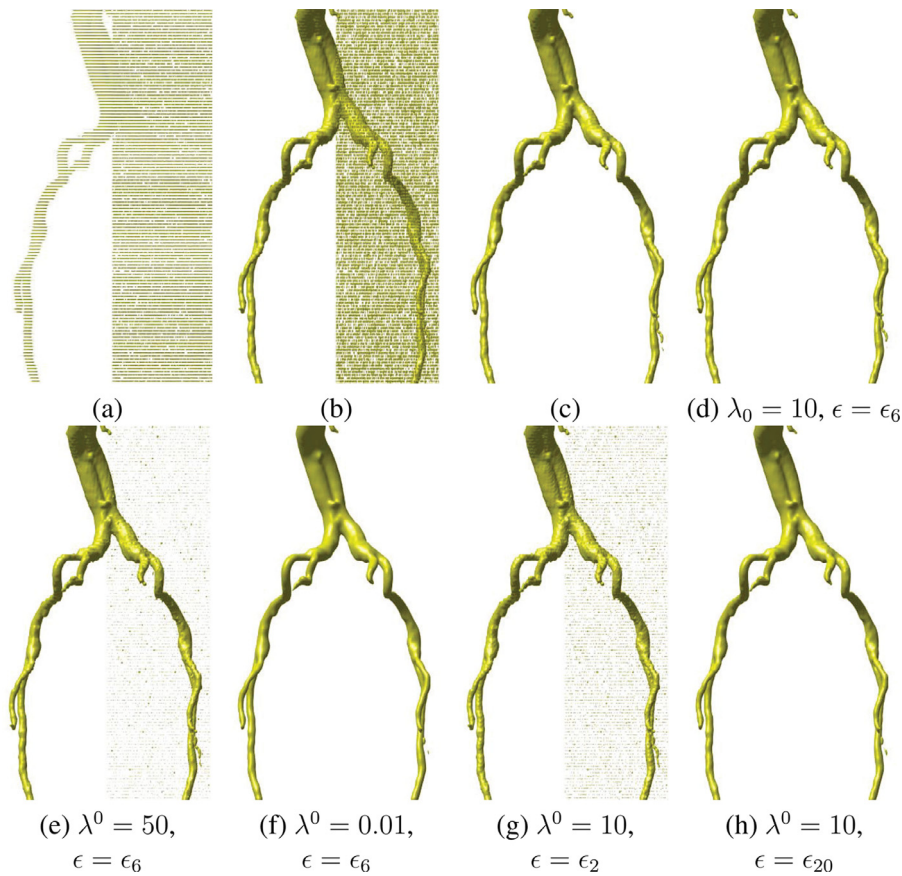
**Fig. 6.** Parameter sensitivity analysis for $\lambda^0$ and $\epsilon$. (a) slice data with 5% salt and pepper noises. (b) initial shape with the interpolation. (c) exact solution. (d-h) reconstructed volumes with different parameters. The adopted parameters are shown below each figure.
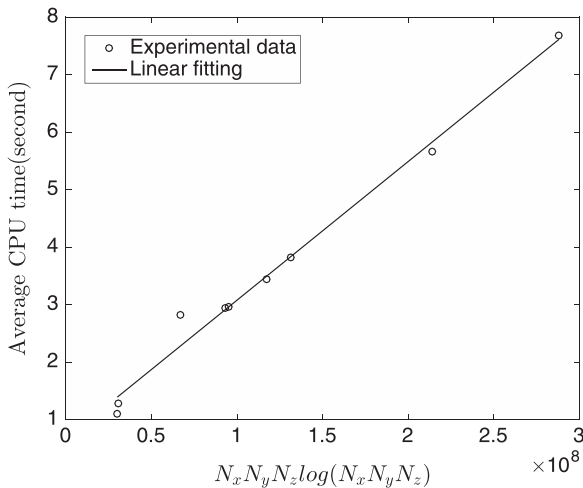


**Fig. 7.** The average CPU time (seconds) vs $N_x N_y N_z \log(N_x N_y N_z)$.

(circle) and the numerical (solid) solutions in different planes. We can see that the numerical results agree with the theoretical values.

Second, we consider the multicomponent volume reconstruction from two slice data sets (as shown in Fig. 9(a)), which is a similar test presented in [17]. In [17], Huang et al. compared their results with related multi-labeled methods [15,16], with which it is difficult to create a single connected green structure that tunnels through the yellow structure. Huang's method [17] created a

geometrically valid material interface with the desired genus for both labels. Our method also simultaneously satisfies the topological requirements as shown in Fig. 9(b)–(d). The comparison with Huang's method [17] is in some way unfair because the algorithm in [17] allows the human-computer interaction, such as by scribbling. On the other hand, our approach can obtain the similar results with simply solving the governing partial differential equations. Furthermore, the advantage of this approach is easy to implementation and is guaranteed to produce well volume, because only a partial differential equation should be solved. As a result, our method can be incorporated into other processing, for example volume segmentation and object recognition. A Fourier-spectral method is performed for the discrete equation, therefore higher computational efficiency can be obtained as shown in Table 1 and Fig. 7. Our method is also compatibility with other numerical methods such as finite difference method, finite element method, finite volume method, etc.

Next, we consider five 3D linked tori, which are labeled with different colors. Twenty-six slice data sets are used, and we insert five slices between any two consecutive slice data sets. The results are shown in Fig. 10. From left to right, the first and second two figures show the initial shapes obtained by linear interpolation and the final result for our proposed method, respectively. As can be obtained in Fig. 10, we obtain a smoothly linked volume.

Next, we consider the effect of the number of slice data sets. From the exact solution defined on the uniform domain and shown in Fig. 11(a), we can choose different numbers of slice data sets as the initial shape. We can fill the missing slices and reconstruct the volume using the proposed method. Fig. 11(b)–(d) show the numerical solutions with 105, 53, and 35 slice data sets, respectively.
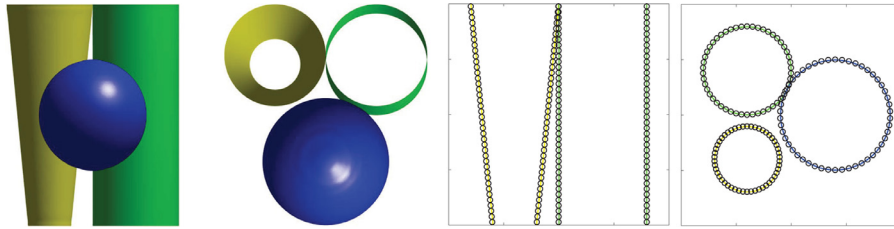
**Fig. 8.** Accuracy test for our method. From left to right, the first two figures show the zero-isosurface of the numerical solution from different views. The second two figures present a comparison between the reference (circle) and numerical (solid) solutions in different planes.
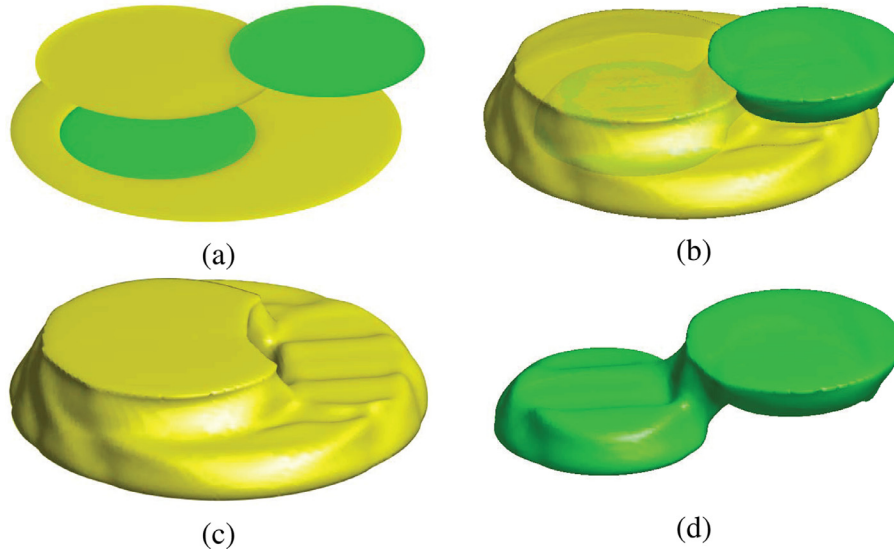


**Fig. 9.** Comparison of a related multi-labeled method. (a) input two given slices. (b-d) volume reconstructed with our method in the whole domain and divided domain. Note that a similar test was performed in [17].
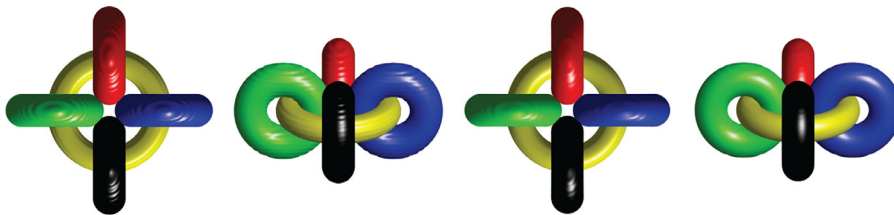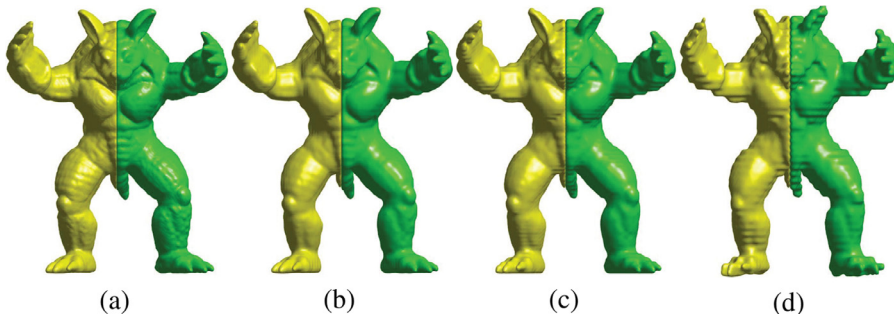


**Fig. 10.** Volume reconstruction for five 3D linked tori. From left to right, the first and second figures show the initial shapes obtained by linear interpolation and the final result for our proposed method, respectively.



**Fig. 11.** Comparison results with different numbers of slice data sets. (a) the exact solution on the uniform domain. (b), (c), and (d) show the reconstructed volumes with 105, 53, and 35 slice data sets, respectively.

For a small number of slice data sets, the solution is not of a high quality. However, its qualitative correctness demonstrates the robustness and efficiency of our proposed method. Furthermore, we can observe that as the number of slice data sets increases, the structure of the armadillo becomes more sharply pronounced, and is much closer to the exact solution.

Fig. 12 presents our reconstruction results for the dragon model. Beginning with the same slice data as shown in Fig. 12(a), we can reconstruct the volume on different mesh grids. The mesh grids in Fig. 12(b) and (c) are of size $236 \times 342 \times 54$ and $236 \times 342 \times 162$, respectively. The results suggest that even with a coarse grid we can obtain a reasonably good reconstructed volume.
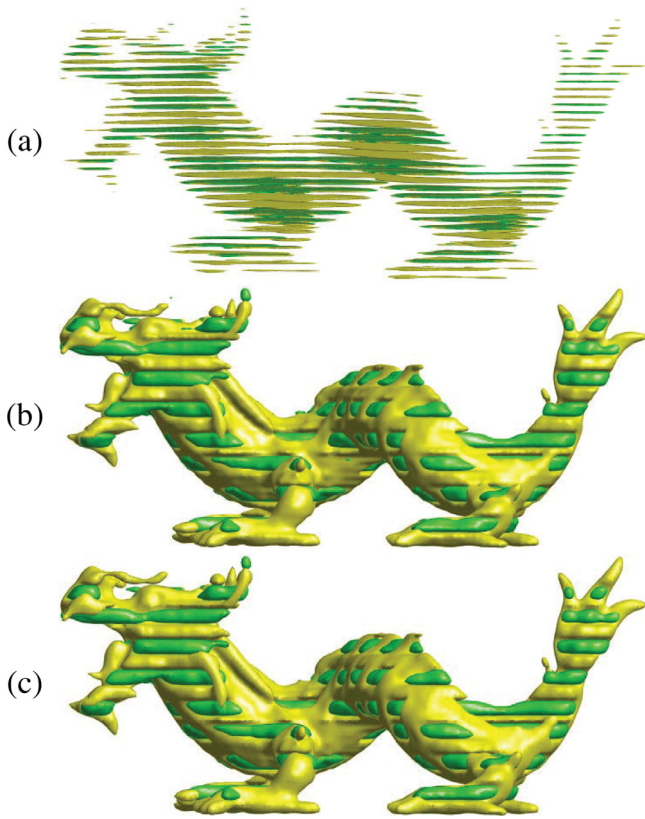
**Fig. 12.** Reconstruction results for the dragon model. (a) slice data. (b) reconstructed volume on a $236 \times 342 \times 54$ mesh grid. (c) reconstructed volume on a $236 \times 342 \times 162$ mesh grid.

In Fig. 13, we illustrate the volume reconstruction for slice data with 10% random noise. Fig. 13(a) and (b) display the exact solution and slice data with 10% random noise, respectively. Fig. 13(c) and (d) show the initial shape with interpolation and the
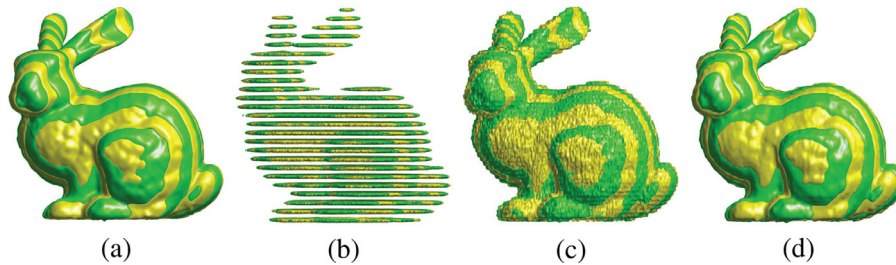
reconstructed volume, respectively. We observe that the noise in the bunny is effectively removed, and the resulting volumes are smooth.

Fig. 14 shows the reconstructed volumes of triply-periodic minimal surfaces, which have constant constant mean curvature everywhere on the surface. Because the geometry of a triply periodic minimal surface strongly influences the physical properties of the material, the triply-periodic minimal surface has been widely employed for natural or man-made structures [34]. We generated initial configurations with the desired topology and 0.5 volume fraction using a modified Allen–Cahn equation [35]. Let $\hat{\phi}_1$ and $\hat{\phi}_2$ denote the volume of the Schwarz diamond and Schoen's F-RD minimal surface, respectively. Then, we define the concentrations of the two components $\phi_1$ and $\phi_2$ as follows:

$$\phi_1 = \begin{cases} 1 - \hat{\phi}_2, & \text{if } \hat{\phi}_1 > 0.05 \text{ and } \hat{\phi}_1 + \hat{\phi}_2 > 1, \\ \hat{\phi}_1, & \text{otherwise.} \end{cases} \tag{15}$$

$$\phi_2 = \hat{\phi}_2. \tag{16}$$

We choose 33 slices as the given slice data. There are three slices between any two consecutive slices except for the first two sets, between which we use two slices. The results in Fig. 14 suggest that our proposed method can perform well for triply-periodic minimal surfaces. The green and yellow regions represent the Schwarz diamond and Schoen's F-RD minimal surface, respectively.

The volume reconstruction results for a dragon model, which has complex topology structures, are presented in Fig. 15. We observe that our proposed method can easily handle the complex geometric shapes, and the reconstructed volume is smooth.

Finally, we demonstrate the performance of our algorithm on the thoracic organ data set. As shown in Fig. 16(a), the input slice data are not well defined as some labels are created in image segmentation processing. As shown in Fig. 16(b), the result demonstrates the ability of our algorithm to smoothly reconstruct a complex anatomical shape with real data sets.



**Fig. 13.** Volume reconstruction for the slice data with 10% random noise. (a) exact solution. (b) slice data with 10% random noises. (c) initial shape with interpolation. (d) reconstructed volume.
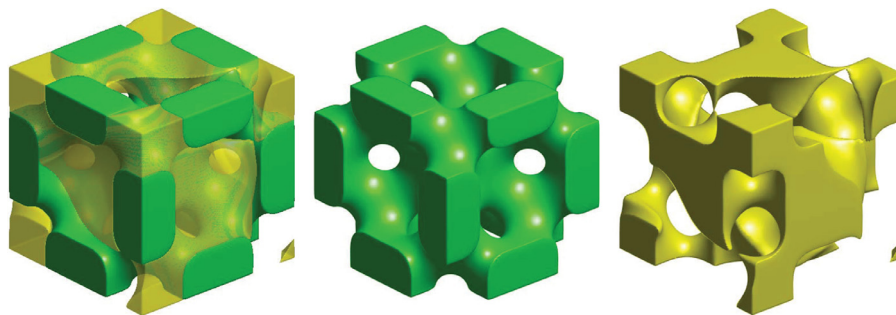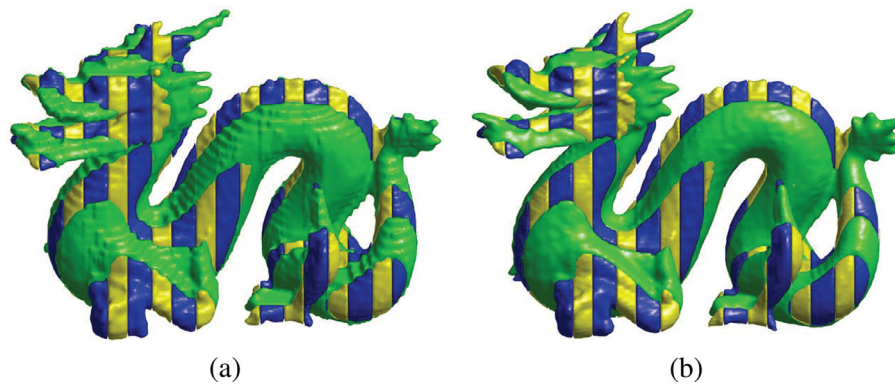


**Fig. 14.** Volume reconstruction results of triply-periodic minimal surfaces. From left to right, we present the multicomponent volumes in the whole domain and divided domain, respectively. The green and yellow regions represent the Schwarz diamond and Schoen's F-RD minimal surface, respectively. (For interpretation of the references to color in this figure legend, the reader is referred to the web version of this article.)

**Fig. 15.** Volume reconstruction results of the dragon model. (a) initial shape with interpolation. (b) reconstructed volume.
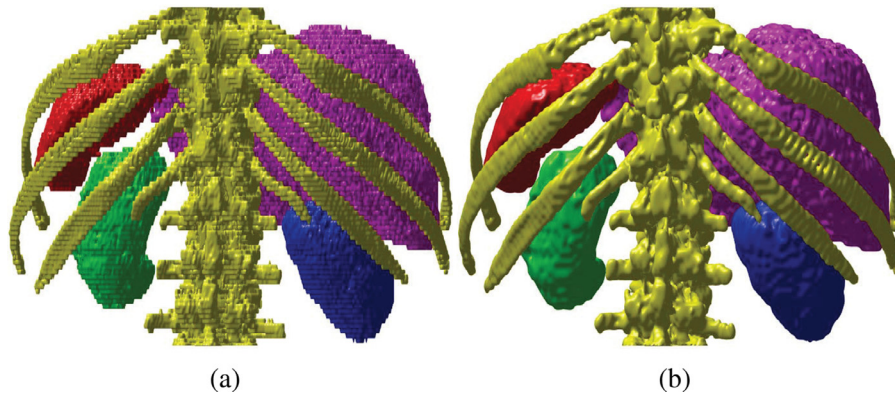


**Fig. 16.** The thoracic organ data set. (a) initial shape with interpolated volume. (b) reconstruction.

## 6. Conclusion

We have proposed an efficient and robust algorithm to reconstruct the volumes of multi-labeled objects from sets of cross sections. The proposed algorithm can handle cross sections in which different regions are classified as having different labels. The present study represents an extension of our previous work [11], in which we modified the original CH equation by adding a fidelity term to keep the solution close to the single-labeled slice data. The CH equation is defined on $\mathbf{R}^3$, and achieves a smoothing effect so that we obtain a smooth interpolating volume. The key idea of the present work is to reconstruct multicomponent volumes without self-intersections or gaps. The proposed numerical method, based on operator splitting techniques, can employ a large time-step size. Our algorithm is simple to implement. Many experimental results have demonstrated the effectiveness of the proposed method. In its current form, the algorithm creates a smooth surface and reduces outliers or noise, but it is difficult to achieve a high accuracy on a sharp surface. It should be noted that the solution to the CH equation is in $[0-\delta, 1+\delta]$, where $\delta$ is a small value related to the thickness $\epsilon$ [27,28]. As $\epsilon \rightarrow 0$, $\delta$ will become zero. In practical simulations, $\epsilon$ should not be too small. In future work, we will present a modified multiphase CH equation that is strictly contained in the interval [0, 1]. Furthermore, to speed up the computation and improve the accuracy of the numerical solution, we will investigate a GPU implementation, develop an adaptive mesh refinement solver for the current algorithm, and apply the four-color labeling method [36]. Another interesting direction for future research would be to reconstruct multicomponent volumes from unorganized planar cross sections.

## References

[1] J. Cheng, Y. Liu, 3-d reconstruction of medical image using wavelet transform and snake model, J. Multimedia 4 (6) (2009) 427–434.

[2] J. Dornheim, D.J. Lehmann, L. Dornheim, B. Preim, G. Strauß, Reconstruction of blood vessels from neck CT datasets using stable 3d mass-spring models, in: Eurographics Workshop on Visual Computing for Biology and Medicine, EG VCBM, 2008, pp. 77–82.

[3] J.F. Guo, Y.L. Cai, Y.P. Wang, Morphology-based interpolation for 3d medical image reconstruction, Comput. Med. Imaging Graph. 19 (3) (1995) 267–279.

[4] W.C. Lin, S.Y. Chen, C.T. Chen, A new surface interpolation technique for reconstructing 3d objects from serial cross-sections, Comput. Vis. Graph. Image Process. 48 (1) (1989) 124–143.

[5] M.W. Jones, M. Chen, A new approach to the construction of surfaces from contour data, in: Computer Graphics Forum, 13, Blackwell Science Ltd., 1994, pp. 75–84.

[6] J.D. Boissonnat, P. Memari, Shape reconstruction from unorganized cross sections, in: Proceedings of the 5th Eurographics Symposiumon Geometry Processing (SGP'07), Barcelona, Spain, 2007, pp. 89–98.

[7] S.P. Raya, J.K. Udupa, Shape-based interpolation of multidimensional objects, IEEE Trans. Med. Imaging 9 (1) (1990) 32–42.

[8] L. Liu, C. Bajaj, J.O. Deasy, D.A. Low, T. Ju, Surface reconstruction from non-parallel curve networks, in: Computer Graphics Forum, 27, Blackwell Publishing Ltd., 2008, pp. 155–163.

[9] S. Deng, Y. Li, L. Jiang, Y. Cao, J. Zhang, Surface reconstruction from sparse & arbitrarily oriented contours in freehand 3d ultrasound, J. Comput. 8 (5) (2013) 1279–1285.

[10] O. Sharma, N. Agarwal, Signed distance based 3d surface reconstruction from unorganized planar cross-sections, Comput. Graph. 62 (2017) 67–76.

[11] Y. Li, J. Shin, Y. Choi, J. Kim, Three-dimensional volume reconstruction from slice data using phase-field models, Comput. Vis. Image Understanding 137 (2015) 115–124.

[12] J.W. Cahn, J.E. Hilliard, Free energy of a nonuniform system I. Interfacial free energy, J. Chem. Phys. 28 (2) (2004) 258–267.

[13] A.L. Bertozzi, S. Esedoglu, A. Gillette, Inpainting of binary images using the Cahn–Hilliard equation, IEEE Trans. Image Process. 16 (1) (2007) 285–291.

[14] E. Bretin, F. Dayrens, S. Masnou, Volume reconstruction from slices, SIAM J. Imaging Sci. 10 (4) (2017) 2326–2358.

[15] A. Bermano, A. Vaxman, C. Gotsman, Online reconstruction of 3d objects from arbitrary cross-sections, ACM Trans. Graph. 30 (5) (2011) 113:1–14

[16] M. Zou, M. Holloway, N. Carr, T. Ju., Topology-constrained surface reconstruction from cross-sections, ACM Trans. Graph. 34 (4) (2015) 1–10.

[17] Z. Huang, M. Zou, N. Carr, T. Ju, Topology-controlled reconstruction of multilabelled domains from cross-sections, ACM Trans. Graph. 36 (4) (2017) 1–12.

[18] R. Lazar, N. Dym, Y. Kushinsky, Z. Huang, T. Ju, Y. Lipman, Robust optimization for topological surface reconstruction, ACM Trans. Graph. 37 (4) (2018) 1–10.

[19] Y. Li, J. Kim, Multiphase image segmentation using a phase-field model, Comput. Math. Appl. 62 (2011) 737–745.

[20] Y. Li, J. Kim, An unconditionally stable numerical method for bimodal image segmentation, Appl. Math. Comput. 219 (6) (2012) 3083–3090.

[21] Y. Li, J. Kim, An unconditionally stable hybrid method for images segmentation, Appl. Numer. Math. 82 (2014) 32–43.

[22] A. Rodtook, K. Kirimasthong, W. Lohitvisate, S.S. Makhanov, Automatic initialization of active contours and level set method in ultrasound images of breast abnormalities, Pattern Recognit. 79 (2018) 172–182.

[23] X.H. Zhi, H.B. Shen, Saliency driven region-edge-based top down level set evolution reveals the asynchronous focus in image segmentation, Pattern Recognit. 80 (2018) 241–255.

[24] M. Zhang, C. Desrosiers, C. Zhang, Atlas-based reconstruction of high performance brain MR data, Pattern Recognit. 76 (2018) 549–559.

[25] J. Kim, S. Lee, Y. Choi, S.M. Lee, D. Jeong, Basic principles and practical applications of the Cahn–Hilliard equation, Math. Probs. in Eng. (2016) 1–11. 2016 Article ID 9532608.

[26] D. Lee, J.Y. Huh, D. Jeong, J. Shin, A. Yun, J. Kim, Physical, mathematical, and numerical derivations of the Cahn–Hilliard equation, Comput. Mater. Sci. 81 (2014) 216–225.

[27] Y. Li, J.I. Choi, J. Kim, Multi-component Cahn–Hilliard system with different boundary conditions in complex domains, J. Comput. Phys. 323 (2016) 1–16.

[28] Y. Li, J.I. Choi, J. Kim, A phase-field fluid modeling and computation with interfacial profile correction term, Commun. Nonlinear. Sci. Numer. Simulat. 30 (2016) 84–100.

[29] H.G. Lee, J.W. Choi, J. Kim, A practically unconditionally gradient stable scheme for the n-component Cahn–Hilliard system, Physica A 391 (4) (2012) 1009–1019.

[30] J.R. Green, A Comparison of Multiphase Models and Techniques, Ph.d. thesis, The University of Leeds, 2007.

[31] L. Cherfils, H. Fakih, A. Miranville, A Cahn–Hilliard system with a fidelity term for color image inpainting, J. Math. Imaging Vision 54 (1) (2016) 117–131.

[32] D.J. Eyre, An unconditionally stable one-step scheme for gradient systems, 1998. Unpublished article. http://www.math.utah.edu/eyre/research/methods/stable.ps.

[33] G. Sheng, T. Wang, Q. Du, K.G. Wang, Z.K. Liu, L.Q. Chen, Coarsening kinetics of a two phase mixture with highly disparate diffusion mobility, Commun. Comput. Phys. 8 (2010) 249–264.

[34] J. Klinowski, A.L. Mackay, H. Terrones, Curved surfaces in chemical structure, Phil. Trans. R. Soc. Lond. A 354 (1715) (1996) 1975–1987.

[35] Y. Li, S. Guo, Triply periodic minimal surface using a modified Allen–Cahn equation, Appl. Math. Comput. 295 (2017) 84–94.

[36] K. Li, W. Tao, X. Liu, L. Liu, Iterative image segmentation with feature driven heuristic four-color labeling, Pattern Recognit. 76 (2018) 69–79.

**Yibao Li** received the B.S. degree from the Department of Mathematics, Xi'an University of Technology, China in 2007. He also received the M.S. and Ph.D. degrees in Applied Mathematics from Korea University, Korea, in 2011 and 2013, respectively. Before he joined the School of Mathematics and Statistics, Xi'an Jiaotong University, China in 2014, he held a research position in Department of Computational Science and Engineering, Yonsei University, Korea. He is currently an associate professor at the Department of Applied Mathematics. His research interests include image processing, computational fluid dynamics, and scientific computing.

**Jing Wang** is an expert of Hundred-Talent Program (Shaanxi Province). Dr. Wang currently is a Director Assistant at National Innovation Institute of Additive Manufacturing. His research interests focused on Additive Manufacturing (3D Printing)? Photoacoustic Microscopy (PAM) Imaging, Multimodal Biomedical Imaging, and Medical Fundus Diseases Detection and Optical Function Imaging System. He was awarded "Assistant Research Award of Wisconsin State University" and "Management contribution award of Science Advancement of Chinese Academy of Sciences".

**Bingheng Lu** received the Ph.D. degree from Xi'an Jiaotong University, Xi?an, China, in 1986. He is an Academician of Chinese Academy of Engineering. Prof. Lu currently is the Director of the National Engineering Research Center for Rapid Manufacturing and the Director of the Highend Collaborative Innovation Center, Xi?an Jiaotong University. His research interests include Additive Manufacturing (3D Printing) and Micro/Nano Manufacturing. He was awarded the national "5.1"Labor Medal by All-China Federation of Trade Unions, the Scientific and Technological Achievement Award of Global Chinese by Hong Kong Chiang fund.

**Darae Jeong** received her Ph.D. in Applied Mathematics from Korea University, Korea, in 2013. And she received M.S. degree in Applied Mathematics and B.S. degree in Mathematics from Korea University in 2011 and Dongguk University in 2008, respectively. She is currently an assistant professor at the Department of Mathematics of Kangwon National University. Her research interests include computational finance, computational fluid dynamics, and scientific computation.

**Junseok Kim** received his Ph.D. in Applied Mathematics from the University of Minnesota, U.S.A. in 2002. He also received his B.S. degree from the Department of Mathematics Education, Korea University, Korea in 1995. He joined the faculty of Korea University, Korea in 2008 where he is currently a professor at the Department of Mathematics. His research interests are in image processing and computational fluid dynamics.